Rare Met. (2023) 42(1):165–175
https://doi.org/10.1007/s12598-022-02118-7

RARE METALS

ORIGINAL ARTICLE

Synergistic effect of bimetallic RuPt/TiO_2 catalyst in methane combustion

Shi-Ying Cao, Fan Ye, Ni-Ni Zhang, Yang-Long Guo, Yun Guo, Li Wang, Sheng Dai, Wang-Cheng Zhan*

Received: 23 February 2022 / Revised: 21 March 2022 / Accepted: 24 March 2022 / Published online: 18 October 2022

Abstract Designing metal compounds based on their structure and chemical composition is essential in achieving desirable performance in methane oxidation, because of the synergistic effect between different metal elements. Herein, a bimetallic Ru–Pt catalyst on TiO_2 support (RuPt-O/TiO_2) was prepared by in situ reduction followed by calcination in air. Compared with monometallic catalysts (Ru-O/TiO_2 and Pt-O/TiO_2), the synergistic effect of mixed metals endowed bimetallic catalysts with excellent stability and outstanding performance in methane oxidation, with a reaction rate of 13.9×10^{-5} $mol_{CH_4}^{-1} \cdot g_{(Ru+Pt)}^{-1} \cdot s^{-1}$ at 303 °C. The varied characterization results revealed that among the bimetallic catalysts, RuO_2 was epitaxially grown on the TiO_2 substrate owing to lattice matching between them, and part of the PtO_x adhered to the RuO_2 surface, in addition to a single PtO_x nanoparticle with 4 nm in size. Consequently, Pt mainly existed in the form of Pt^{2+} and Pt^{4+} and a small amount of zero valence in the bimetallic catalyst, prompting the adsorption and activation of methane as the first and rate-controlling step for CH_4 oxidation. More importantly, the RuO_2 species provided additional oxygen species to facilitate the redox cycle of the PtO_x species. This study opens a new route for structurally designing promising catalysts for CH_4 oxidation.

Keywords Synergistic effect; Bimetallic catalyst; Methane combustion; Redox cycle

1 Introduction

Natural gas (> 90% CH_4 content) is an attractive energy source due to its abundance and high energy density (high H/C ratio). However, the release of unburned CH_4 during flame combustion can pose serious environmental problems because of the strong greenhouse effect of CH_4 that is twenty times greater than that of CO_2 at the same molar amount [1]. The catalytic combustion of methane is regarded as the most promising method for reducing the emissions of CH_4 in industrial processes at relatively low temperatures (~ 500 °C), with the advantages of high combustion efficiency and low emission of other toxic products, such as NO_x [2]. Nevertheless, this method requires the development and screening of high-performance catalysts.

Noble metal catalysts (such as Pt, Pd and Rh) are widely used for methane combustion due to their high catalytic activity at low temperatures [3–7]. These catalytic activities are mainly dependent on the dispersion and electronic structure of the noble metal and the properties of the support. Although encouraging progress has been made in improving the catalytic performance of CH_4 oxidation, the reliability of CH_4 oxidation at low temperatures is still

Supplementary Information The online version contains supplementary material available at https://doi.org/10.1007/s12598-022-02118-7.

S.-Y. Cao, N.-N. Zhang, Y.-L. Guo, Y. Guo, L. Wang, W.-C. Zhan*
Key Laboratory for Advanced Materials and Research Institute of Industrial Catalysis, School of Chemistry and Molecular Engineering, East China University of Science and Technology, Shanghai 200237, China
e-mail: zhanwc@ecust.edu.cn

F. Ye, S. Dai
Key Laboratory for Advanced Materials and Feringa Nobel Prize Scientist Joint Research Centre, Institute of Fine Chemicals, School of Chemistry and Molecular Engineering, East China University of Science and Technology, Shanghai 200237, China

unclear. Recently, bimetallic catalysts have been exploited in CH_4 oxidation because of their unique synergistic and electronic effects, especially Pd–Pt catalysts. Chetyrin et al. [8] reported that during CH_4–O_2 catalysis, single Pt atoms and small Pt clusters dispersed on an Al_2O_3 support are largely inactive. In contrast, large Pt–Pd alloy clusters (> 5 nm) with a thin PdO shell covering a Pt-rich core dispersed on an Al_2O_3 support are highly reactive. On these cluster surfaces, the O^{2-} anions are highly nucleophilic, whereas the Pd^{2+} cations are highly electrophilic because they are in contact with the underlying Pt-rich core. These form Pd^{2+}–O^{2-} site pairs that catalyze the kinetically relevant C–H bond cleavage of CH_4 via the formation of a highly stabilized four-center transition state ($H_3C^{\delta-}$–Pd^{2+}–$H^{\delta+}$–O^{2-}) more effectively than monometallic O*-covered Pt or PdO clusters [9, 10]. In contrast, Ru-based catalysts are utilized less for CH_4 combustion, mainly because of their poor high-temperature stability [11]. However, Ru–Pt bimetallic catalysts have been studied in the field of C_1 catalysis, particularly for methanol electrooxidation reactions (MOR). For example, porous carbon-supported Ru–Pt catalysts prepared via strong electrostatic adsorption and electroless deposition are more active than pure Pt [12]. Moreover, the interaction between Ru and Pt can enhance methanol conversion [13]. There could be a "bifunctional mechanism" in Ru–Pt bimetallic catalysts. In particular, the C–H bond of methanol could be cleaved and CO adsorbed at Pt sites; however, Ru atoms can provide more O species to consume the intermediate poisoning on Pt sites [14, 15]. Although Ru–Pt bimetallic catalysts have been widely used for MOR, limited reports exist on Ru–Pt bimetallic catalysts for CH_4 combustion. However, the properties of support materials generally affect the activity of the supported catalysts. TiO_2 has been widely used as catalyst support, and the crystalline phase of rutile-type TiO_2 matches that of RuO_2, enhancing the high dispersion and stability of the RuO_2 active phase [16, 17]. Herein, a bimetallic RuPt/TiO_2 catalyst precursor was synthesized by an in situ reduction method [14], and then the precursor was oxidized to obtain a catalyst (RuPt-O/TiO_2) with a stable structure. The various characterizations demonstrated that both PtO_x particles (4 nm) and twinned noble metal structures were present on the RuPt-O/TiO_2 catalyst, that is, RuO_2 was epitaxially grown on the TiO_2 substrate and PtO_x adhered to the RuO_2 surface. As a result, the Pt species in the bimetallic RuPt-O/TiO_2 catalyst consisted of Pt^{2+} and Pt^{4+}, while Pt^0 was present in the Pt-O/TiO_2 catalyst. The synergistic effect of RuO_2 and PtO_x species afforded superior CH_4 oxidation performance on RuPt-O/TiO_2 catalyst. PtO_x can prompt CH_4 activation and oxidation, and RuO_2 species can provide additional oxygen species to PtO_x to furnish the redox cycle of PtO_x species. Consequently, the performance of RuPt-O/TiO_2 catalyst in CH_4 oxidation was significantly enhanced compared with that of the corresponding monometallic catalysts.

2 Experimental

2.1 Catalysts preparation

The rutile-type TiO_2 purchased from Shanghai Macklin Biochemical Co., Ltd. was used as support. The bimetallic catalyst was synthesized by the produces described in Ref. [14]. First, a certain amount of TiO_2 was added into 20 ml H_2O and then ultrasonicated for 30 min. Second, a certain amount of $H_2PtCl_6{\cdot}6H_2O$ and $RuCl_3$ were added into the suspension liquid and ultrasonicated for 30 min again. Then, the suspension liquid was placed in a water bath of 50 °C and kept continuously stirring until the solvents were evaporated. The sample was dried at 60 °C overnight in a vacuum oven, and then was reduced under 10 vol% H_2/Ar at 300 °C for 3 h. Afterward, the as-prepared sample was washed and centrifuged repeatedly with deionized water to wash away residual ions and then dried at 60 °C overnight in a vacuum oven. Finally, the sample was reduced to under 10 vol% H_2/Ar at 700 °C for 3 h, which was labeled as RuPt/TiO_2.

On this basis, the RuPt/TiO_2 was calcined at 500 °C in air for 1 h, which was labeled as RuPt-O/TiO_2. The monometallic Ru-O/TiO_2 and Pt-O/TiO_2 catalysts were synthesized by the same produces. The theoretical total metal loading of all catalysts was 1 wt%, and the atomic ratio of Ru/Pt in the bimetallic catalyst was 1.

2.2 Catalysts characterization

The loading of metal was detected by inductively coupled plasma-atomic emission spectroscopy (ICP-AES, Agilent 725ES). X-ray diffraction (XRD) patterns were detected on a Bruker D8 Focus diffractometer with Cu Kα radiation (λ = 0.154056 nm, 40 kV and 40 mA), scanning from 10° to 80° at a speed of 6 (°)·min^{-1}. The surface areas of catalysts were obtained on the Quantachrome Nova Touch LX3 instrument at − 196 °C and were calculated by the Brunauer–Emmett–Teller (BET) method. Laser Raman spectra of catalysts were obtained on a Renishaw Raman spectrometer at ambient condition, and the 532 nm line of a spectra physics Ar^+ laser was used as an excitation. Electron paramagnetic resonance (EPR) measurements were performed on a Bruker EMX-8/2.7 EPR Spectrometer. Aberration-corrected scanning transmission electron microscopy (AC-STEM) characterization was performed using a ThermoFisher Themis Z electron microscope. High-angle annular dark-field (HAADF)-STEM images were recorded using a convergence semi-angle of 0.6303°,

and inner- and outer collection angles of 3.381° and 11.46°, respectively. Energy-dispersive X-ray spectroscopy (EDS) was carried out using 4-in-column Super-X detectors. X-ray photoelectron spectra (XPS) of all the catalysts were detected on a Thermo ESCALAB 250Xi spectrometer equipped with Al Kα (1486.6 eV) radiation as the excitation source. All binding energies (BE) were determined with respect to the C 1s line (284.8 eV) originating from adventitious carbon.

In situ diffuse reflectance and infrared Fourier transform spectra (DRIFTS) of CH_4 adsorption on the catalysts were measured on a Nicolet Nexus 6700 spectrometer with an MCT detector, and the sample cell was equipped with ZnSe windows. DRIFT spectra were collected with a resolution of 4 cm^{-1} and 64 scans in Kubelka–Munk units. The catalysts were pretreated at 500 °C for 1 h in Ar, and then were exposed to the feed gas consisting of 20 vol% CH_4/N_2 (0.5 $ml{\cdot}min^{-1}$) balanced by Ar (49.5 $ml{\cdot}min^{-1}$) at 350 °C. DRIFT spectra were recorded for 0, 1, 3, 5, 10 and 20 min under the continued feed gas.

CH_4/O_2 pulse experiments were carried out on a Micromecitics Auto II 2920 instrument with a mass spectrometer (HPR-20 QIC). The specific test process was similar to that described in Ref. [3]. The catalysts (50 mg) were pretreated in a 3 vol% O_2/He with a flow rate of 40 $ml{\cdot}min^{-1}$ at 400 °C for 1 h. After cooling down to 350 °C, the catalyst was purged with He at 350 °C for 30 min. Then a stream of 5 vol% CH_4/Ar was injected into the catalyst for ten pulses with a precise analytical syringe (loop volume 0.5173 ml) until the baseline remained stable. CH_4 (mass-to-charge ratio of *m*/e = 15), CO_2 (*m*/e = 44), CO (*m*/e = 29), H_2 (*m*/e = 2) and O_2 (*m*/e = 32) were continuously recorded by a mass spectrometer. After ten pulses were injected, the catalysts were purged with He for 20 min, and then a stream of 3 vol% O_2/He was injected into the catalyst for ten pulses. Similarly, the catalysts were purged with He for 20 min. The above is a cycle. Therefore, CH_4/O_2 pulse measurements were conducted by repeatedly dosing 5 vol% CH_4/Ar or 3 vol% O_2/He into the catalyst bed at 350 °C.

2.3 Catalytic performances measurements

The catalytic activity of all the catalysts for CH_4 combustion was tested in a fixed bed quartz reactor at atmospheric pressure. 200 mg catalysts (40–60 mesh) was used. The feed gas consisted of 1 vol% CH_4, 20 vol% O_2 and N_2 balanced with a flow rate of 50 $ml{\cdot}min^{-1}$, and the gas hourly space velocity (GHSV) was 15,000 $ml{\cdot}g^{-1}{\cdot}h^{-1}$. The catalyst bed was heated from 150 to 500 °C at a rate of 3 $°C{\cdot}min^{-1}$, and the CH_4 concentrations were detected by an online gas chromatograph (Agilent GC 7890A) equipped with thermal conductivity detectors (TCD). The selectivity of CO_2 was close to 100% over the catalysts, and the other possible products were under the detective limit of the GC.

The reaction rate of the catalysts in CH_4 oxidation was also measured in the feed gas consisted of 1 vol% CH_4, 20 vol% O_2, and N_2 balanced. The GHSV was 15,000 and 60,000 $ml{\cdot}g^{-1}{\cdot}h^{-1}$ for the monometallic and bimetallic catalysts, respectively, to achieve the conversion of CH_4 lower than 5%–15%. The reaction rates (r_{CH_4}) were calculated by the following equation:

$$r_{CH_4} = \frac{C_{CH_4} X_{CH_4} V P_{atm}}{m_{cat} w_M R T} \quad (1)$$

where C_{CH_4} is the concentration of CH_4 in the feed gas; X_{CH_4} is the conversion of CH_4; m_{cat} is the mass of the catalyst used; w_M is the loading of metal; P_{atm} is the atmosphere pressure, equaled to 101.3 kPa; R is the molar gas constant, equaled to 8.314 Pa $m^3{\cdot}mol^{-1}{\cdot}K^{-1}$; T is the room temperature, equaled to 25 °C.

3 Results and discussion

3.1 Catalyst structure

The structures of the RuPt/TiO_2 catalysts were first investigated. Figure 1 shows the aberration-corrected HAADF–STEM images and corresponding EDS elemental maps of the RuPt/TiO_2 sample reduced at 700 °C. Two types of particles of distinct sizes were identified in the catalyst (Fig. 1a). The sizes of most small particles were ~ 4.0 nm, and the *d*-spacing of {111} was 0.243 nm, as shown in Fig. 1a, b. Compared with the standard lattice parameter of Pt, it can be determined that this phase should be Pt, which is further demonstrated by EDS result in Fig. 1f, g. In contrast, the size of large particles was ~ 10.0 nm, and the structure is face-centered cubic (fcc) with the *d*-spacing around 0.216 nm for {111} planes, e.g., the measured values of 0.216, 0.217 and 0.214 nm in Fig. 1c–e. Based on the contracted lattice constant and the uniform distribution of Pt and Ru in the EDS maps (Fig. 1f–i), it can be concluded that the large nanoparticles are Pt–Ru alloys. Owing to a large difference in the reduction potential and crystal lattice between Pt and Ru [18, 19], Ru–Pt alloys are difficult to obtain through facile synthesis.

Figure 2 shows HAADF–STEM images and corresponding EDS elemental maps (Fig. 2b–e) of RuPt-O/TiO_2 catalyst oxidized in air at 500 °C. Small Pt particles still existed and the size did not change significantly from ~ 4.0 nm (Fig. 2a). However, the size and structure of the Ru–Pt bimetallic nanoparticles (NPs) changed after calcination in air for 1 h. Ru was oxidized to RuO_2 and

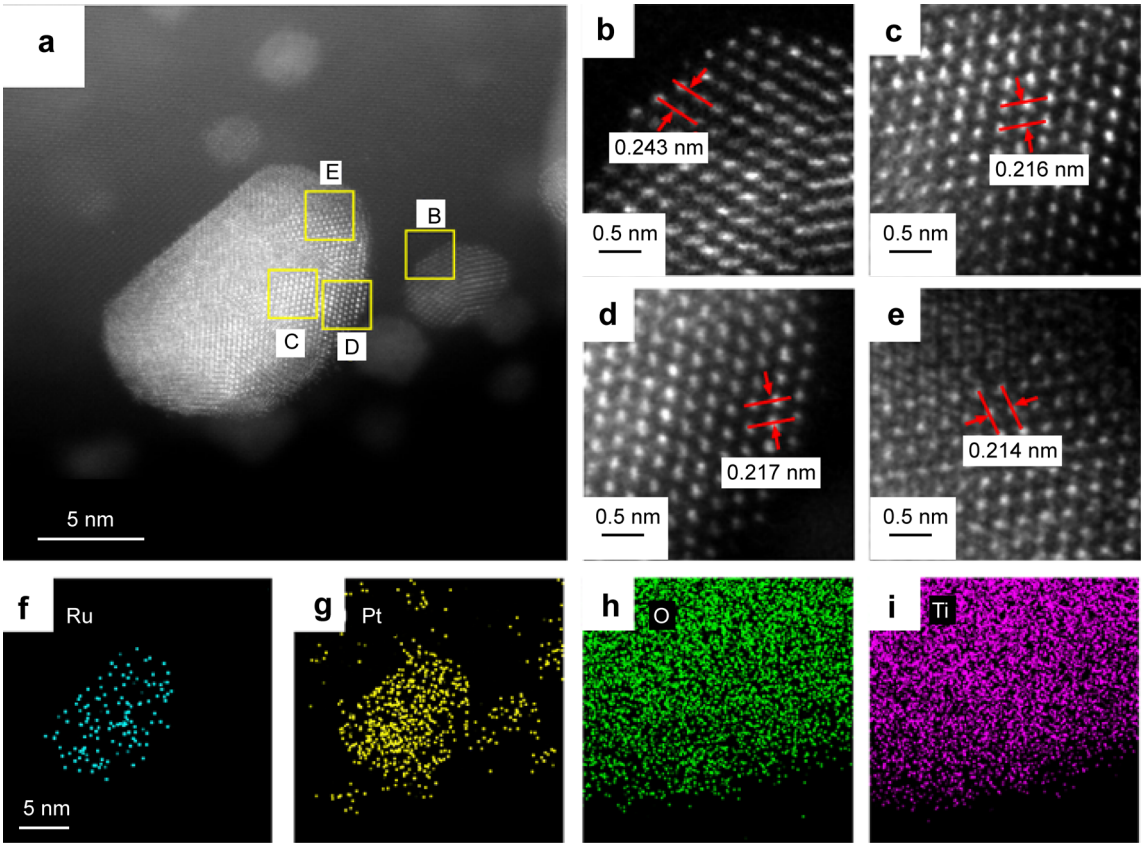

Fig. 1 **a** HAADF–STEM image; **b–e** enlarged images of B–E regions marked by yellow boxes in **a**; **f–i** EDS elemental maps of RuPt/TiO_2 sample corresponding to region shown in **a**

epitaxially grown on TiO_2 substrate due to lattice matching between them, and PtO_x adheres to RuO_2 surface. A fast Fourier transform (FFT) image of the TiO_2 matrix is shown in the inset of Fig. 2a, demonstrating the tetragonal structure of TiO_2 crystal along [111] zone axis. Compared with the standard structure of RuO_2, it can be determined that the region marked by the red circle in Fig. 2f was a single crystal of RuO_2 with a tetragonal structure in the [111] direction (the FFT of this region is shown in Fig. 2g), whose orientation and lattice parameters were almost the same as those of the TiO_2 matrix. Notably, EDS elemental maps showed phase separation of Pt and Ru in the RuPt-O/TiO_2 catalyst. The atomic-scale HAADF–STEM image also shows a varied Z-contrast, indicating the different regions of PtO_x and RuO_2, which was different from that of Pt–Ru alloy. This was also verified by the measured lattice distances in Fig. 2f, which showed Pt-rich region (0.358 nm) and RuO_2 region (0.349 nm).

Figures S1 and S2 show HAADF–STEM images and corresponding EDS elemental maps of monometallic Ru-O/TiO_2 and Pt-O/TiO_2, respectively. The particle size of Ru and Pt was $\sim$ 11.3 and 5.2 nm with a broad size distribution, respectively. The size of the Pt NPs was similar to that of the Pt in RuPt-O/TiO_2 catalyst.

Briefly, both Pt and bimetallic Ru–Pt NPs were present in the bimetallic RuPt-O/TiO_2 catalyst after calcination at 500 °C for 1 h in air. Although the relative proportions of both NPs could not be identified, the special structure of the bimetallic RuPt-O/TiO_2 catalyst could provide unique catalytic activity compared with the monometallic Pt and Ru catalysts [20–22].

XRD patterns of Ru-O/TiO_2, Pt-O/TiO_2 and RuPt-O/TiO_2 catalysts are shown in Fig. 3. All catalysts exhibited diffraction peaks corresponding to rutile-type TiO_2 (JCPDS No. 21-1276) [23]. In addition, XRD pattern of Ru-O/TiO_2 catalyst showed a diffraction peak at $2\theta = 35.1°$, which was assigned to the (101) crystalline planes of RuO_2 (JCPDS No. 70-2662). In contrast, XRD pattern of Pt-O/TiO_2 catalyst showed no diffraction peaks assigned to Pt and PtO_x due to its small particle size (5.2 nm), as observed by transmission electron microscopy (TEM). No diffraction peaks attributed to Pt and Ru were observed in XRD pattern of the bimetallic RuPt-O/TiO_2 catalyst due to the relatively small particle sizes of both PtO_x and Ru–Pt bimetallic NPs (Fig. 2).

Figure 4a shows Raman spectra of Ru-O/TiO_2, Pt-O/TiO_2 and RuPt-O/TiO_2 catalysts. The vibration bands of the rutile-type TiO_2 were located at 136, 229, 442 and

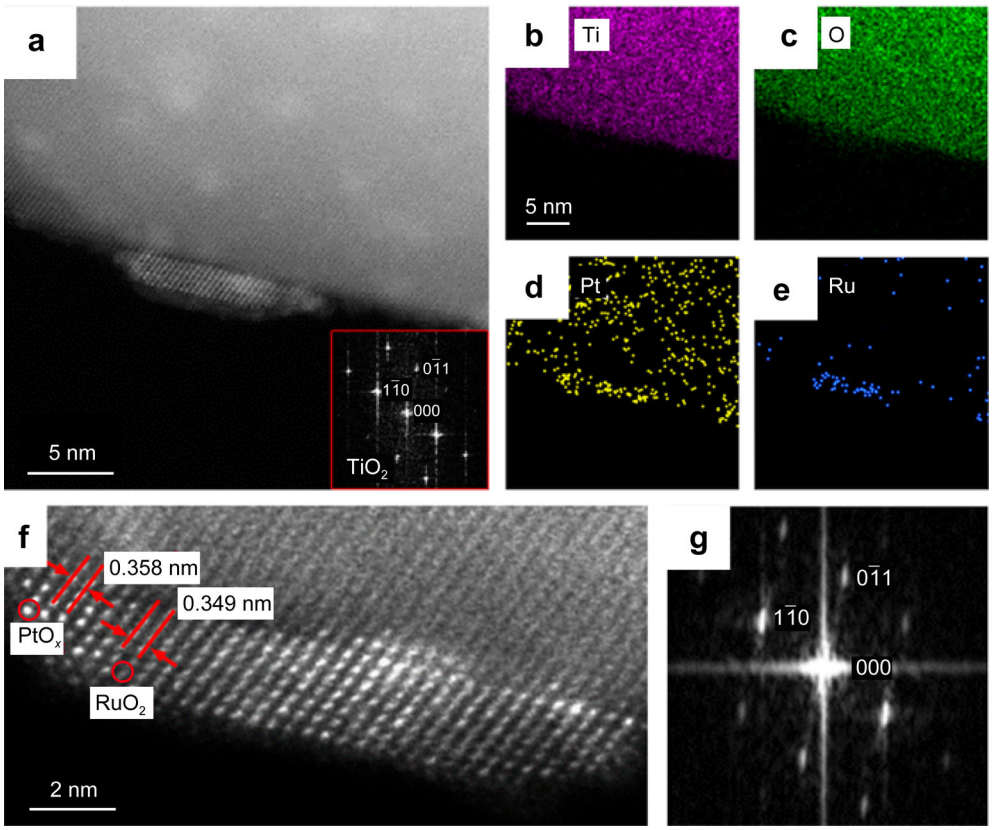

Fig. 2 **a, f** HAADF–STEM images, **b–e** corresponding EDS elemental maps and **g** FFT patterns of RuPt-O/TiO_2 catalyst

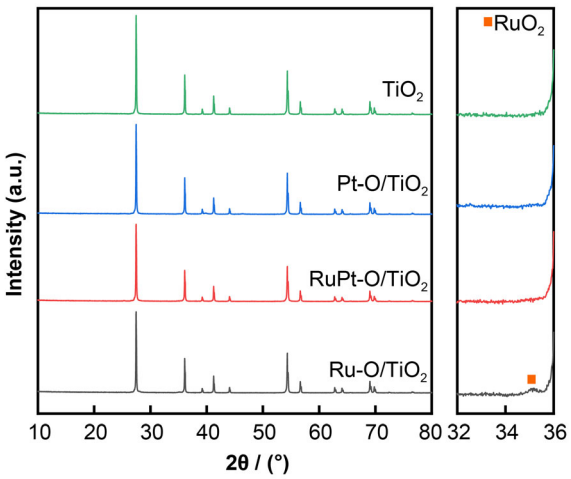

Fig. 3 XRD patterns and enlarged view of the corresponding pattern of TiO_2, Ru-O/TiO_2, Pt-O/TiO_2 and RuPt-O/TiO_2 catalysts

605 cm^{-1}, which correspond to the classical B_{1g}, two-photon scattering process, E_g (planar O–O vibration), and A_{1g} (Ti–O stretch) Raman modes, respectively [24]. All catalysts exhibited similar spectra and an obvious red-shift of the E_g mode compared to the support TiO_2, indicating that a large number of defects were present in TiO_2 and decreased after NP loading. Moreover, the amounts of defects in Ru-O/TiO_2 and RuPt-O/TiO_2 catalysts were lower than those in Pt-O/TiO_2 catalyst, due to the epitaxial growth of RuO_2 on the TiO_2 substrate that consumed more surface defects. This conclusion was further confirmed by EPR spectra. As shown in Fig. 4b, all the catalysts and the support TiO_2 showed a signal at $g = 2.006$ (g is a constant of proportionality, whose value is the property of the electron in a certain environment), which was assigned to surface oxygen vacancies [25]. The signal intensity for the support TiO_2 was stronger than that for the catalysts, indicating that a large number of surface oxygen vacancies were present on the support TiO_2, and they were consumed by NP loading to a certain degree. Moreover, the decrease was more pronounced for Ru-O/TiO_2 and RuPt-O/TiO_2 catalysts, which is consistent with Raman results. In summary, metal NPs tended to be located in oxygen vacancies on the support TiO_2, and Ru and Pt–Ru loading consumed more surface defects due to the epitaxial growth of RuO_2 on TiO_2 substrate.

3.2 CH_4 oxidation performance of catalyst

After determining the catalyst structure, its catalytic performance in methane oxidation was determined. Figure 5 shows the methane conversion as a function of temperature

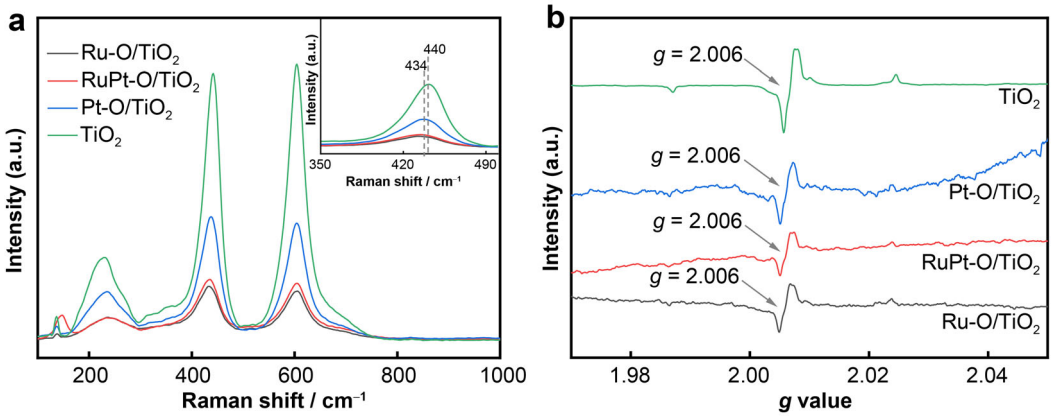

Fig. 4 **a** Laser Raman and **b** EPR spectra of Ru-O/TiO_2, Pt-O/TiO_2 and RuPt-O/TiO_2 catalysts

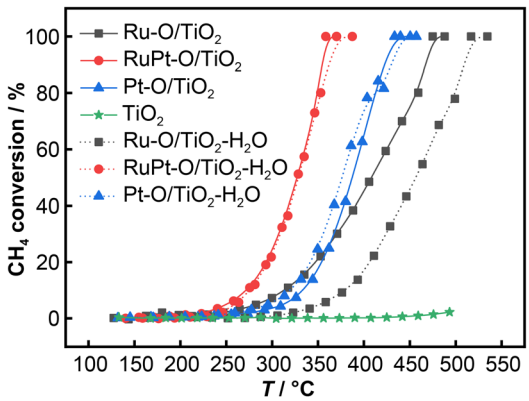

Fig. 5 Catalytic activity of Ru-O/TiO_2, Pt-O/TiO_2 and RuPt-O/TiO_2 catalysts for CH_4 combustion in dry condition (solid line) and wet condition containing 5 vol% H_2O (dot line), where feed gas consisted of 1 vol% CH_4, 20 vol% O_2, 5 vol% H_2O (when used), and N_2 balance, and GHSV was 15,000 $ml \cdot g^{-1} \cdot h^{-1}$

on the support TiO_2, monometallic Pt-O/TiO_2, Ru-O/TiO_2, and bimetallic RuPt-O/TiO_2 catalysts. The support TiO_2 was inert for methane oxidation. After loading Pt and Ru, the catalytic performance in methane oxidation was significantly enhanced, and methane was completely converted on the Pt-O/TiO_2 and Ru-O/TiO_2 catalysts at 450 and 490 °C, respectively. The bimetallic RuPt-O/TiO_2 catalyst with a constant total loading of 1 wt% of Pt and Ru showed excellent catalytic activity for methane oxidation. The temperature for complete methane conversion declined to 357 °C, which was much lower than that for both Pt-O/TiO_2 and Ru-O/TiO_2 catalysts. More importantly, after the addition of 5 vol% H_2O to the feed gas, the bimetallic RuPt-O/TiO_2 catalyst could preserve the activity of methane oxidation, but the Ru-O/TiO_2 catalyst showed a low ability to H_2O resistance.

To further confirm the catalytic activities of the catalysts, the reaction rates were determined, and the results are listed in Table S1. The reaction rate of the bimetallic RuPt-O/TiO_2 catalyst was estimated based on the fact that both Ru and Pt species were involved in methane oxidation. The reaction rate for CH_4 oxidation was 13.9×10^{-5} over the RuPt-O/TiO_2 catalyst at 303 °C, and it was 1.55×10^{-5} and 1.59×10^{-5} $mol_{CH_4}^{-1} \cdot g_{(Ru+Pt)}^{-1} \cdot s^{-1}$ over Ru-O/TiO_2 and Pt-O/TiO_2 catalysts, respectively, confirming the superior activity of the bimetallic RuPt-O/TiO_2 catalyst for methane oxidation compared with the monometallic catalysts.

The stability of the catalysts for CH_4 combustion was also evaluated. As shown in Fig. 6a, both Ru-O/TiO_2 and RuPt-O/TiO_2 catalysts maintained their catalytic activities during the three reaction cycles, indicating reasonable stability. However, the catalytic activity of Pt-O/TiO_2 catalyst improved slightly during the three reaction cycles, which can be attributed to the activation process during the first cycle as it is typical for Pt-based catalysts [26]. The stability of the catalysts during long-term oxidation reactions was further evaluated. As shown in Fig. 6b, both Ru-O/TiO_2 and RuPt-O/TiO_2 catalysts exhibited high stability, and methane conversion was maintained at 16% and 85% within 30 h, respectively. Curiously, the methane conversion on Pt-O/TiO_2 catalyst gradually increased from 32% to 55% within 5 h and then remained constant, possibly because of the formation of an active layer of strongly adsorbed oxygen species during the reaction [26], which was represented in three reaction cycles on the Pt-O/TiO_2 catalyst.

3.3 Nature of activity difference between catalysts

XPS spectra were obtained to explore the chemical states of Pt and Ru in the catalyst as crucial parameters for methane oxidation. As shown in Fig. 7a, the Ti 2p spectra of all catalysts consisted of two individual peaks at BE = 464.4 and 458.7 eV, and the peaks of Ti $2p_{3/2}$ and Ti $2p_{1/2}$ showed a difference of ~ 5.7 eV, which was consistent

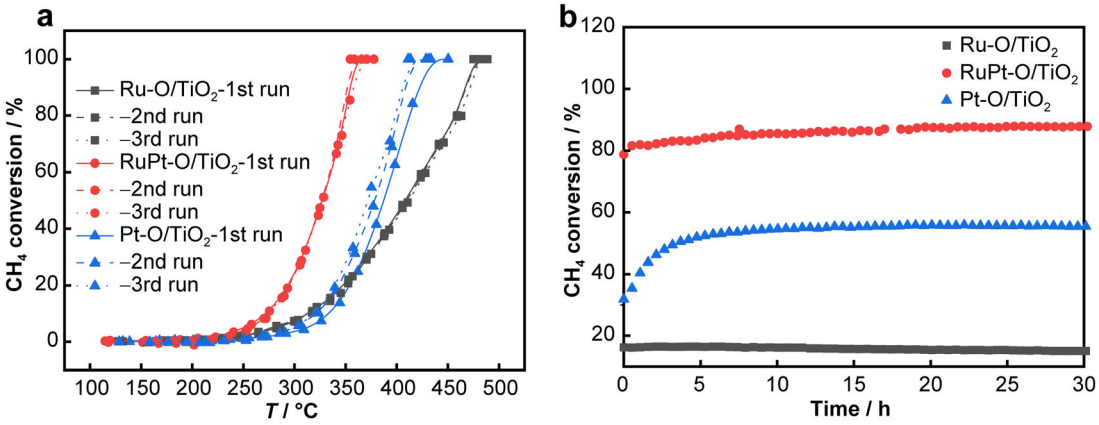

Fig. 6 Stability of Ru-O/TiO_2, Pt-O/TiO_2, and RuPt-O/TiO_2 catalysts during **a** recycling experiments and **b** prolonged oxidation at 350 °C, where feed gas consisted of 1 vol% CH_4, 20 vol% O_2, and N_2 balance, and GHSV was 15,000 $ml \cdot g^{-1} \cdot h^{-1}$

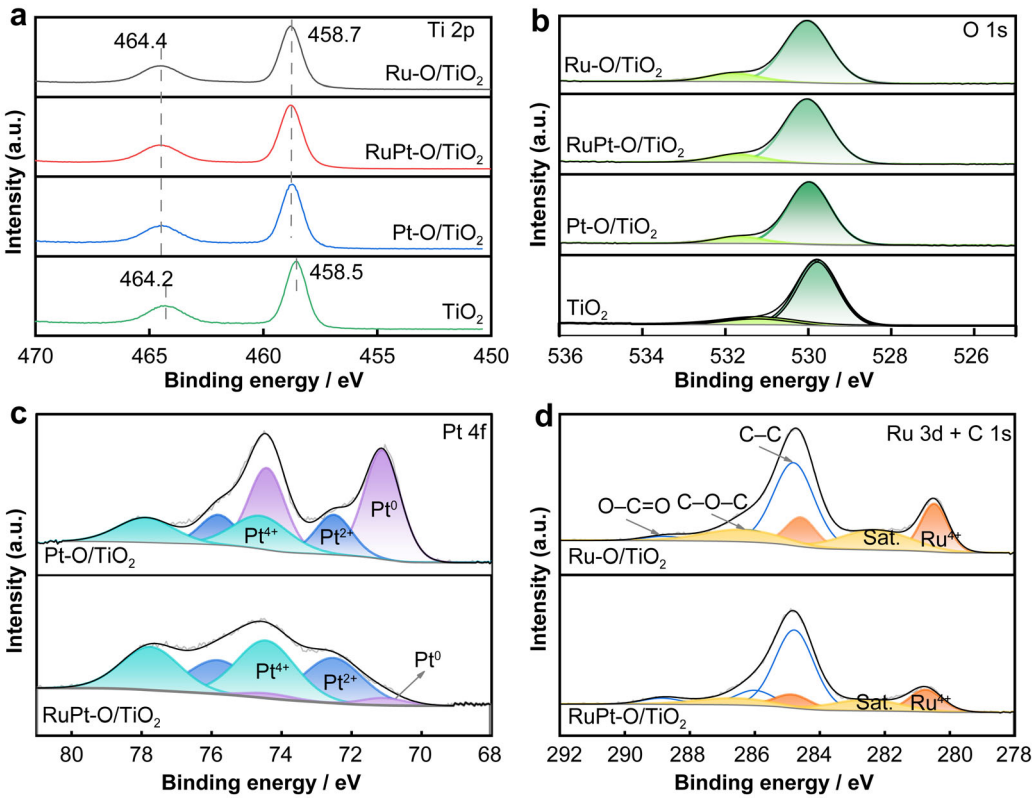

Fig. 7 **a** Ti 2p, **b** O 1s, **c** Pt 4f, and **d** Ru 3d XPS spectra of Ru-O/TiO_2, Pt-O/TiO_2, and RuPt-O/TiO_2 catalysts

with the state of Ti^{4+}, indicating the presence of Ti^{4+} in all catalysts [27, 28]. Ti 2p peaks of Ru-O/TiO_2, Pt-O/TiO_2, and RuPt-O/TiO_2 shifted to a higher binding energy than those of TiO_2, indicating that TiO_2 possessed a lower valence state, which resulted from more oxygen vacancies available on the support TiO_2. The O 1s spectra of all the catalysts can be divided into two peaks (Fig. 7b). The two peaks at 529–530 and 532 eV were assigned to lattice oxygen (O_{lat}) and surface-adsorbed oxygen (O_{ads}), respectively [29–31]. The ratio of O_{ads}/O_{lat} was calculated using the peak area ratio of O_{ads} to O_{lat}. The ratios of the four catalysts were very similar: Pt-O/TiO_2 (0.13) ≈ RuPt-O/TiO_2 (0.14) ≈ Ru-O/TiO_2 (0.15) ≈ TiO_2 (0.18).

Pt 4f XPS spectra of Pt-O/TiO_2 and RuPt-O/TiO_2 catalysts were deconvoluted (Fig. 7c). XPS spectrum the Pt-O/TiO_2 catalyst included three components of Pt^0, Pt^{2+} and Pt^{4+}, and the metallic Pt (Pt^0) at BE = 70.9 and 74.2 eV was a bare majority [32]. Pt species in the bimetallic RuPt-O/TiO_2 catalyst also consisted of Pt^0, Pt^{2+} and Pt^{4+}. However, the ratio of Pt^0/Pt on RuPt-O/TiO_2 catalyst

(5.1%) was significantly lower than those on Pt-O/TiO_2 catalyst (42.3%), as shown in Table S1. The significant difference in Pt valence between Pt-O/TiO_2 and RuPt-O/TiO_2 catalysts can be attributed to the hybrid bimetallic NP in RuPt-O/TiO_2 catalyst. The presence of a RuO_2 transition layer between TiO_2 and PtO_x in RuPt-O/TiO_2 catalyst can significantly inhibit the decomposition of PtO_x to Pt during the calcination process, leading to a small amount of metallic Pt. Regarding Ru 3d spectrum (Fig. 7d), the bands at ~ BE = 280.5 and 284.6 eV were assigned to Ru^{4+}, and those at ~ BE = 282.2 and 286.3 eV were assigned to the satellite peaks of RuO_2 [33–35]. Therefore, both the monometallic Ru-O/TiO_2 and bimetallic RuPt-O/TiO_2 catalysts exhibited Ru^{4+}, indicating no difference in Ru valence between them. Summarily, there was only a difference in the valence state of Pt among the three catalysts.

Regarding CH_4 combustion, the adsorption of CH_4 molecules and dissociation of C–H bonds on the surface of precious metal oxides (PtO_x and RuO_x) is the first rate-controlling step, followed by the gradual oxidation of CH_3 by O from precious metal oxides to form CO_2 and H_2O, accompanied by the reduction of metal oxides, such as PtO to $Pt^{\delta+}$ ($0 < \delta < 2$). Subsequently, the metal oxides are directly re-oxidized to their initial states by both active O atoms on the surface of the support and gas-phase O_2 [36–38]. Therefore, CH_4 adsorption and activation, as well as the redox cycle of precious metal oxides, were determined by DRIFT spectra of CH_4 adsorption and CH_4/O_2 pulse experiments, respectively.

Figure 8 shows DRIFT spectra of CH_4 adsorption on Ru-O/TiO_2, Pt-O/TiO_2, and RuPt-O/TiO_2 catalysts. Regarding the spectra on Ru-O/TiO_2 catalyst, the absorption bands assigned to gaseous methane appeared at 1300, 2953, 3019 and 3095 cm^{-1} after exposure for 1 min. Meanwhile, there were two weak bands at 2330 and 2360 cm^{-1} assigned to gaseous CO_2 [39]. Increasing the exposure time of CH_4 to 5 min, the intensity of both weak bands increased significantly, due to CH_4 adsorption and oxidation on the catalyst. In addition, the new band at 2009 and 2078 cm^{-1} appeared for 5 min, assigned to CO linear adsorption (Ru-(CO)) and twin adsorption (Ru-$(CO)_3$) on Ru species [40, 41]. With a further increase in the exposure time to 20 min, the intensity of all bands slightly increased. Overall, CH_4 was adsorbed and oxidized on RuO_2 sites to produce CO_2 on the Ru-O/TiO_2 catalyst, accompanied by the reduction of RuO_2 to $Ru^{\delta+}$ ($2 < \delta < 4$) under O free conditions. Subsequently, the oxidation ability decreased, and an incomplete oxidation product of CO was generated and adsorbed on $Ru^{\delta+}$ species.

DRIFT spectra for CH_4 adsorption on Pt-O/TiO_2 catalysts were significantly different from those on Ru-O/TiO_2 catalysts. As shown in Fig. 8b, after exposure for 1 min, there were two intense absorption bands at 3019 and 2069 cm^{-1}, which were assigned to gaseous CH_4 and CO linearly adsorbed on metallic Pt, respectively [22]. CO is produced only from the incomplete oxidation of CH_4. In addition, two weak absorption bands assigned to gaseous CO_2 appeared at 2330 and 2360 cm^{-1}. With an increase in the exposure time of CH_4 to 20 min, the intensities of all the bands did not change significantly. Combined with the spectra of Ru-O/TiO_2 catalyst, it can be seen that Pt-O/TiO_2 catalyst has a higher ability to activate and oxidize CH_4. However, a significantly higher amount of CO than CO_2 was produced on Pt-O/TiO_2 catalyst due to the low valence state of Pt, as shown in XPS results.

As shown in Fig. 8c, for the spectra of RuPt-O/TiO_2 catalyst, all bands assigned to gaseous CH_4, gaseous CO_2, and CO linearly adsorbed on metallic Pt and Ru appeared for an exposure time of 1 min. Compared with the spectra of both monometallic catalysts for an exposure time of 1 min, the amount of CO_2 produced increased significantly, accompanied by a marked decrease in the amount of CO linearly adsorbed on metallic Pt. Furthermore, with an increase in the exposure time of CH_4 to 20 min, the intensities of these bands increased slightly. This superior CH_4 oxidation performance was ascribed to the synergistic effect of the RuO_2 and PtO_x species based on the special structures of PtO_x adhered to the RuO_2 surface. Firstly, compared with Pt-O/TiO_2 catalyst, the higher valence state of Pt can prompt CH_4 activation. Secondly, RuO_2 species

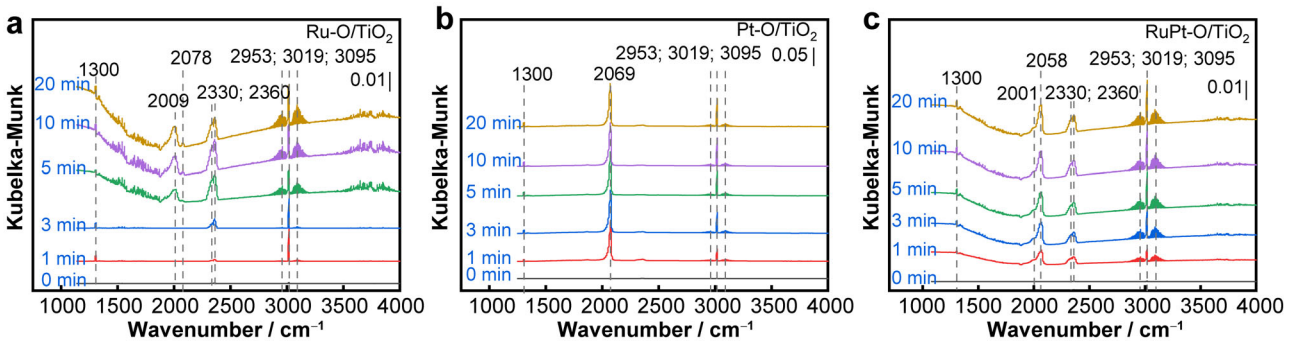

Fig. 8 In situ DRIFT spectra of CH_4 adsorption over **a** Ru-O/TiO_2, **b** Pt-O/TiO_2, and **c** RuPt-O/TiO_2

could provide additional oxygen species to oxidize CO adsorbed on metallic Pt to CO_2, furnishing the redox cycle of PtO_x species.

To further confirm the redox cycle on the catalyst surface, a CH_4 or O_2 pulse was applied at 350 °C on Ru-O/TiO_2, Pt-O/TiO_2, and RuPt-O/TiO_2 catalysts. After ten pulses of CH_4 or O_2 during every cycle were injected, the total amount of CH_4 and O_2 consumed was calculated and is represented by a bar in Fig. 9. The amount of CH_4 consumed over Ru-O/TiO_2 (5.7 $\mu mol \cdot g^{-1}$) and Pt-O/TiO_2 (15.7 $\mu mol \cdot g^{-1}$) catalysts in the first cycle of CH_4 pulses was much lower than that observed for RuPt-O/TiO_2 catalyst (50.0 $\mu mol \cdot g^{-1}$), demonstrating that RuPt-O/TiO_2 catalyst possessed more active oxygen species to convert CH_4. Both CO and CO_2 were detected as products formed during the CH_4 pulse, being consistent with in situ DRIFT spectra of CH_4 adsorption. Subsequently, ten O_2 pulses were injected to replenish the oxygen species consumed in the CH_4 pulses, leading to re-oxidation of Pt and Ru species. The amount of O_2 consumed over RuPt-O/TiO_2 catalyst was 4.4 $\mu mol \cdot g^{-1}$, which was higher than that consumed over Ru-O/TiO_2 (0.5 $\mu mol \cdot g^{-1}$) and Pt-O/TiO_2 (1.4 $\mu mol \cdot g^{-1}$) catalysts, due to the low amount of CH_4 consumed in CH_4 pulses for the monometallic catalysts. In the second cycle of CH_4 pulses, the amount of CH_4 consumed over RuPt-O/TiO_2 catalyst slightly decreased to 40.8 $\mu mol \cdot g^{-1}$ and then remained unchanged in the third cycle of CH_4 pulses. These results indicate that the O species consumed in the cycle of CH_4 pulses can be recovered by O_2 pulses on RuPt-O/TiO_2 catalyst, that is, the re-oxidation of Pt and Ru species, leading to the reservation of a high amount of CH_4 consumption for CH_4 pulses in the subsequent cycles. Similarly, the amount of CH_4 consumed in the second cycle of CH_4 pulses over Pt-O/TiO_2 catalyst decreased and then remained unchanged in the third cycle of CH_4 pulses. However, the amount of CH_4 consumed was significantly lower than that consumed by RuPt-O/TiO_2 catalyst. Regarding Ru-O/TiO_2 catalyst, the amounts of CH_4 consumed in three cycles of CH_4 pulses were quite close to each other and were significantly lower than those consumed by both RuPt-O/TiO_2 and Pt-O/TiO_2 catalysts.

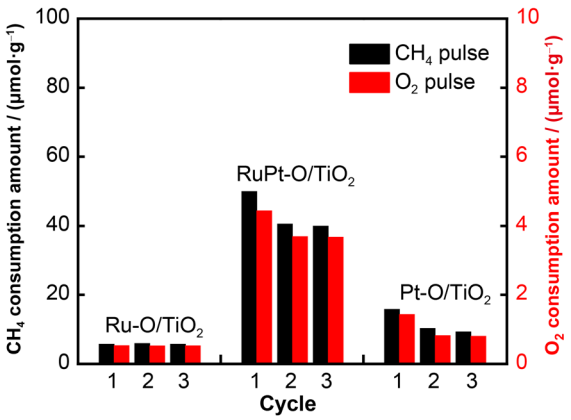

Fig. 9 CH_4 and O_2 pulse experiments on Ru-O/TiO_2, Pt-O/TiO_2, and RuPt-O/TiO_2 catalysts, where specific columns represent total amount of CH_4 or O_2 consumed for ten pulses during each cycle

In summary, RuPt-O/TiO_2 catalyst possessed a high amount of active oxygen species on the catalyst surface, and a relatively stable redox cycle of RuO_x and PtO_x species was achieved. In contrast, Ru-O/TiO_2 catalyst had a significantly lower amount of active O species on the catalyst surface, although it exhibited the most stable redox cycle of the catalyst. The superior redox cycle of RuPt-O/TiO_2 catalyst was attributed to the synergistic effect of RuO_2 and PtO_x species based on the special structures of PtO_x adhered onto RuO_2 surface, as in the case of CH_4 adsorption and activation on RuPt-O/TiO_2 catalyst.

4 Conclusion

The bimetallic RuPt-O/TiO_2 catalyst was prepared by in situ reduction, followed by calcination in air. Specific Ru and Pt structures were constructed on the RuPt-O/TiO_2 catalyst. RuO_2 was epitaxially grown on a TiO_2 substrate, and part of the PtO_x adhered to the RuO_2 surface, in addition to a single PtO_x nanoparticle with a diameter of 4 nm. Owing to the synergistic effect of Ru and Pt, the RuPt-O/TiO_2 catalyst exhibited superior catalytic activity compared with monometallic Ru-O/TiO_2 and Pt-O/TiO_2 catalysts for CH_4 oxidation. The oxidation reaction rate of the RuPt-O/TiO_2 catalyst at 303 °C was approximately an order of magnitude higher than that of the monometallic catalysts. Moreover, the RuPt-O/TiO_2 catalyst exhibited excellent stability and water resistance. No difference was observed in the valence state of Ru between RuPt-O/TiO_2 and Ru-O/TiO_2 catalysts, but a significant difference was observed in the valence state of Pt between RuPt-O/TiO_2 and Pt-O/TiO_2 catalysts. Pt^{2+} and Pt^{4+} mainly existed on RuPt-O/TiO_2 catalyst and Pt^0 largely presented on Pt-O/TiO_2 catalyst, in addition to Pt^{2+} and Pt^{4+}. Consequently, the adsorption and activation of CH_4 were strengthened on RuPt-O/TiO_2 catalyst. Meanwhile, the RuO_2 species could provide additional oxygen species to facilitate the redox cycle of PtO_x species. Therefore, the bimetallic catalyst was more effective for methane oxidation than monometallic catalysts.

Acknowledgements This study was financially supported by National Natural Science Foundation of China (Nos. 21922602, 22076047 and U21A20326), Shanghai Science and Technology Innovation Action Plan (No. 20dz1204200) and the Fundamental Research Funds for the Central Universities.

Declarations

Conflict of interests The authors declare that they have no conflict of interest.

References

[1] Li JJ, Abbas SU, Wang HQ, Zhang Zhicheng HuWP. Recent advances in interface engineering for electrocatalytic CO_2 reduction reaction. Nano-micro Lett. 2021;13:216. https://doi.org/10.1007/s40820-021-00738-9.

[2] Guo MX, Du JC, Li H, Zhang XJ, Zhang AM, Zhao YK. New research progress on precious metal catalysts for methane combustion. Chin J Rare Met. 2021;45(9):1133. https://doi.org/10.13373/j.cnki.cjrm.XY19110015.

[3] Ding YQ, Wu QQ, Lin B, Guo YL, Guo Y, Wang YS, Wang L, Zhan WC. Superior catalytic activity of a Pd catalyst in methane combustion by fine-tuning the phase of ceria-zirconia support. Appl Catal B-Environ. 2020;266:118631. https://doi.org/10.1016/j.apcatb.2020.118631.

[4] Tang X, Lou Y, Zhao RL, Tang BJ, Guo WY, Guo YL, Zhan WC, Jia YY, Wang L, Dai S, Guo Y. Confinement of sub-nanometric PdCo bimetallic oxide clusters in zeolites for methane complete oxidation. Chem Eng J. 2021;418:129398. https://doi.org/10.1016/j.cej.2021.129398.

[5] Yang XW, Li Q, Lu EJ, Wang ZQ, Gong XQ, Yu ZY, Guo Y, Wang L, Guo Y, Zhan WC, Zhang JS, Dai S. Taming the stability of Pd active phases through a compartmentalizing strategy toward nanostructured catalyst supports. Nat Commun. 2019;10:1611. https://doi.org/10.1038/s41467-019-09662-4.

[6] Zhao ZY, Wang BW, Ma J, Zhan WC, Wang L, Guo Y, Guo YL, Lu GZ. Catalytic combustion of methane over Pd/SnO_2 catalysts. Chin J Catal. 2017;38(8):1322. https://doi.org/10.1016/s1872-2067(17)62864-x.

[7] Cao XQ, Zhou J, Li S, Qin GW. Ultra-stable metal nano-catalyst synthesis strategy: a perspective. Rare Met. 2019;39(2):113. https://doi.org/10.1007/s12598-019-01350-y.

[8] Chetyrin IA, Bukhtiyarov AV, Prosvirin IP, Khudorozhkov AK, Bukhtiyarov VI. In Situ XPS and MS study of methane oxidation on the $Pd\text{-}Pt/Al_2O_3$ catalysts. Top Catal. 2020;63(1–2):66. https://doi.org/10.1007/s11244-019-01217-7.

[9] Nie HY, Howe JY, Lachkov PT, Chin CY. Chemical and structural dynamics of nanostructures in bimetallic Pt-Pd catalysts, their inhomogeneity, and their roles in methane oxidation. ACS Catal. 2019;9(6):5445. https://doi.org/10.1021/acscatal.9b00485.

[10] Yang YF, Lee JY, Dorakhan R, Nie HY, Fu GS, Quarantotto A, Howe JY, Chin CY. Active site structure and methane oxidation reactivity of bimetallic Pd and Pt nanoparticles. Appl Catal A-Gen. 2022;629:118290. https://doi.org/10.1021/j.apcata.2021.118290.

[11] Choudhary TV, Banerjee S, Choudhary VR. Catalysts for combustion of methane and lower alkanes. Appl Catal A-Gen. 2002;234:1. https://doi.org/10.1016/s0926-860x(02)00231-4.

[12] Mehrabadi B, White R, Shakouri A, Regalbuto J, Weidner J, Monnier J. Ruthenium-platinum bimetallic catalysts with controlled surface compositions and enhanced performance for methanol oxidation. Catal Today. 2019;334:156. https://doi.org/10.1016/j.cattod.2018.11.042.

[13] Christensen S, Feng H, Libera J, Guo N, Miller J, Stair P, Elam J. Supported Ru-Pt bimetallic nanoparticle catalysts prepared by atomic layer deposition. Nano Lett. 2010;10(8):3047. https://doi.org/10.1021/nl101567m.

[14] Zhang JM, Qu XM, Han Y, Shen LF, Yin SH, Li G, Jiang YX, Sun SG. Engineering PtRu bimetallic nanoparticles with adjustable alloying degree for methanol electrooxidation: enhanced catalytic performance. Appl Catal B-Environ. 2020;263:118345. https://doi.org/10.1016/j.apcatb.2019.118345.

[15] Qin YC, Wang FQ, Wang XM, Wang MW, Zhang WL, An WK, Wang XP, Ren YL, Zheng X, Lv DC, Ahmad A. Noble metal-based high-entropy alloys as advanced electrocatalysts for energy conversion. Rare Met. 2021;40(9):2354. https://doi.org/10.1007/s12598-021-01727-y.

[16] Kim A, Sanchez C, Patriarche G, Ersen O, Moldovan S, Wisnet A, Sassoye C, Debecker D. Selective CO_2 methanation on Ru/TiO_2 catalysts: unravelling the decisive role of the TiO_2 support crystal structure. Catal Sci Technol. 2016;6(22):8117. https://doi.org/10.1039/c6cy01677d.

[17] Kim A, Debecker D, Devred F, Dubois V, Sanchez C, Sassoye C. CO_2 methanation on Ru/TiO_2 catalysts: on the effect of mixing anatase and rutile TiO_2 supports. Appl Catal B-Environ. 2018;220:615. https://doi.org/10.1016/j.apcatb.2017.08.058.

[18] Gilroy K, Ruditskiy A, Peng HC, Qin D, Xia YN. Bimetallic nanocrystals: syntheses, properties, and applications. Chem Rev. 2016;116(18):10414. https://doi.org/10.1021/acs.chemrev.6b00211.

[19] Zhang ZC, Liu GG, Cui XY, Gong Y, Yi D, Zhang QH, Zhu CZ, Saleem F, Chen B, Lai ZC, Yun QB, Cheng HF, Huang ZQ, Peng YW, Fan ZX, Li B, Dai WR, Chen W, Du YH, Ma L, Sun C-J, Hwang I, Chen SM, Song L, Ding F, Gu L, Zhu YH, Zhang H. Evoking ordered vacancies in metallic nanostructures toward a vacated Barlow packing for high-performance hydrogen evolution. Sci Adv. 2021;7:eabd6647. https://doi.org/10.1126/sciadv.abd6647.

[20] Qin YC, Zhang WL, Wang FQ, Li JJ, Ye JY, Sheng X, Li CX, Liang XY, Liu P, Wang XP, Zheng X, Ren YL, Xu CL, Zhang ZC. Extraordinary p-d hybridization interaction in heterostructural Pd-PdSe nanosheets Boosts C–C bond cleavage of ethylene glycol electrooxidation. Angew Chem Int Ed. 2022. https://doi.org/10.1002/anie.202200899.

[21] Guan QQ, Zhu CW, Lin Y, Vovk E, Zhou XH, Yang Y, Yu HC, Cao L, Wang HW, Zhang XH, Liu XY, Zhang MK, Wei SQ, Li WX, Lu JL. Bimetallic monolayer catalyst breaks the activity-selectivity trade-off on metal particle size for efficient chemoselective hydrogenations. Nat Catal. 2021;4(10):840. https://doi.org/10.1038/s41929-021-00679-x.

[22] Cui MY, Johnson G, Zhang ZY, Li S, Hwang S, Zhang X, Zhang S. AgPd nanoparticles for electrocatalytic CO_2 reduction: bimetallic composition-dependent ligand and ensemble effects. Nanoscale. 2020;12(26):14068. https://doi.org/10.1039/d0nr03203d.

[23] Ma M, Wang H, Liu H. Steering spatially separated dual sites on nano-TiO_2 through SMSI and lattice matching for robust photocatalytic hydrogen evolution. Chin Chem Let. 2021;32(11):3613. https://doi.org/10.1016/j.cclet.2021.04.012.

[24] Nguyen-Phan T, Luo S, Vovchok D, Llorca J, Sallis S, Kattel S, Xu WQ, Piper L, Polyansky D, Senanayake S, Stacchiola D, Rodriguez J. Three-dimensional ruthenium-doped TiO_2 sea urchins for enhanced visible-light-responsive H_2 production. Phys Chem Chem Phys. 2016;18(23):15972. https://doi.org/10.1039/c6cp00472e.

[25] Yan JQ, Wu GJ, Guan NJ, Li LD. Nb_2O_5/TiO_2 heterojunctions: synthesis strategy and photocatalytic activity. Appl Catal B--Environ. 2014;152–153:280. https://doi.org/10.1016/j.apcatb.2014.01.049.

[26] Arzac G, Montes O, Fernández A. Pt-impregnated catalysts on powdery SiC and other commercial supports for the combustion of hydrogen under oxidant conditions. Appl Catal B Environ. 2017;201:391. https://doi.org/10.1016/j.apcatb.2016.08.042.

[27] Bian X, Xiao KY, Wang SH, Qiu BL. Preparation and properties of $x$$CeO_{2-y}$$WO_3$-$TiO_2$ denitrification catalyst. Chin J Rare Met. 2020;44(9):974. https://doi.org/10.13373/j.cnki.cjrm.xy19030020.

[28] Wang HQ, Liu HL, Ji YC, Yang RQ, Zhang ZF, Wang X, Liu H. Hybrid nanostructures of pit-rich TiO_2 nanocrystals with Ru loading and N doping for enhanced solar water splitting. Chem Commun. 2019;55(19):2781. https://doi.org/10.1039/c8cc10093d.

[29] Cui X, Chen L, Wang Y, Chen H, Zhao W, Li Y, Shi J. Fabrication of hierarchically porous RuO_2-CuO/Al-ZrO_2 composite as highly efficient catalyst for ammonia-selective catalytic oxidation. ACS Catal. 2014;4(7):2195. https://doi.org/10.1021/cs500421x.

[30] Liu H, Li X, Dai QG, Zhao HL, Chai T, Guo YL, Guo Y, Wang L, Zhan WC. Catalytic oxidation of chlorinated volatile organic compounds over Mn-Ti composite oxides catalysts: elucidating the influence of surface acidity. Appl Catal B-Environ. 2021;282:119577. https://doi.org/10.1016/j.apcatb.2020.119577.

[31] Chen SL, Abdel-Mageed AM, Li D, Bansmann J, Cisneros S, Biskupek J, Huang WX, Behm RJ. Morphology-engineered highly active and stable Ru/TiO_2 catalysts for selective CO methanation. Angew Chem Int Ed Engl. 2019;58(31):10732. https://doi.org/10.1002/anie.201903882.

[32] Ma Y, Zhang XH, Cao L, Lu JL. Effects of the morphology and heteroatom doping of CeO_2 support on the hydrogenation activity of Pt single-atoms. Catal Sci Technol. 2021;11(8):2844. https://doi.org/10.1039/d0cy02279a.

[33] Wang Z, Huang ZP, Brosnahan JT, Zhang S, Guo YL, Guo Y, Wang L, Wang YS, Zhan WC. Ru/CeO_2 catalyst with optimized CeO_2 support morphology and surface facets for propane combustion. Environ Sci Technol. 2019;53(9):5349. https://doi.org/10.1021/acs.est.9b01929.

[34] Liu H, Yang J, Jia YY, Wang ZQ, Jiang MX, Shen K, Zhao HL, Guo YL, Guo Y, Wang L, Dai S, Zhan W. Significant improvement of catalytic performance for chlorinated volatile organic compound oxidation over RuO_x supported on acid--etched Co_3O_4. Environ Sci Technol. 2021;55(15):10734. https://doi.org/10.1021/acs.est.1c02970.

[35] Weber T, Abb M, Khalid O, Pfrommer J, Carla F, Znaiguia R, Vonk V, Stierle A, Over H. In situ studies of the electrochemical reduction of a supported ultrathin single-crystalline RuO_2(110) layer in an acidic environment. J Phys Chem C. 2019;123(7):3979. https://doi.org/10.1021/acs.jpcc.8b10741.

[36] Oh S, Mitchell P, Siewert R. Methane oxidation over alumina-supported noble metal catalysts with and without cerium additives. J catal. 1991;132:287. https://doi.org/10.1016/0021-9517(91)90149-x.

[37] Zhou GF, Ma J, Bai S, Wang L, Guo Y. CO catalytic oxidation over Pd/CeO_2 with different chemical states of Pd. Rare Met. 2020;39(7):800. https://doi.org/10.1007/s12598-019-01347-7.

[38] Feng Y, Wang CC, Wang C, Huang HB, Hsi H, Duan E, Liu YX, Guo GS, Dai HX, Deng J. Catalytic stability enhancement for pollutant removal via balancing lattice oxygen mobility and VOCs adsorption. J Hazard Mater. 2022;424:127337. https://doi.org/10.1016/j.jhazmat.2021.127337.

[39] Yu XH, Dai LY, Deng JG, Liu YX, Jing L, Zhang X, Gao RY, Hou ZQ, Wei L, Dai HX. An isotopic strategy to investigate the role of water vapor in the oxidation of 1,2-dichloroethane over the Ru/WO_3 or Ru/TiO_2 catalyst. Appl Catal B-Environ. 2022;305:121037. https://doi.org/10.1006/j.apcatb.2021.121037.

[40] Hadjiivanov K, Lavalley J, Lamotte J, Mauge F, Saint-Just J, Che M. FTIR study of CO interaction with Ru/TiO_2 catalysts. J Catal. 1998;176:415. https://doi.org/10.1016/jcat.1998.2038.

[41] Dongapure P, Bagchi S, Mayadevi S, Devi R. Variations in activity of Ru/TiO_2 and Ru/Al_2O_3 catalysts for CO_2 hydrogenation: an investigation by in-situ infrared spectroscopy studies. Mol Catal. 2020;482:110700. https://doi.org/10.1016/j.mcat.2019.110700.